actuators

MDPI

Article

Electromagnetic Characteristics and Preliminary Design of Ultra-High-Speed PMSLMs

Yongpan Hu [1,2], Dinggang Gao [1,2], Tao Wen [3,4], Yuanzhe Zhao [1,2,5,*], Ke Huang [6], Junqi Xu [1,2,5] and Guobin Lin [1,2,5,*]

1 College of Transportation, Tongji University, Shanghai 201804, China; 23310023@tongji.edu.cn (Y.H.); 12138@tongji.edu.cn (D.G.); xujunqi@tongji.edu.cn (J.X.)
2 Key Laboratory of Railway Industry of Maglev Technology, Shanghai 201804, China
3 School of Digital Intelligence Engineering, Xinjiang Vocational and Technical University of Tianshan, Atux City 845350, China; wentao@nudt.edu.cn
4 School of Flight Technology, Jiangxi Flight University, Nanchang 330088, China
5 State Key Laboratory of High-Speed Maglev Transportation Technology, Shanghai 201804, China
6 School of Electrical Engineering, Southwest Jiaotong University, Chengdu 611756, China; huangke202405@my.swjtu.edu.cn
* Correspondence: 22017@tongji.edu.cn (Y.Z.); 12154@tongji.edu.cn (G.L.)

Abstract

The permanent magnet synchronous linear motor (PMSLM) is a key technology for the ultra-high-speed acceleration in maglev transport systems over short distances. It has attracted significant research interest owing to its high power density, high efficiency, and excellent control performance. Nevertheless, the design of such motors faces several challenges. These include the accurate calculation of inductance parameters and the achievement of high thrust force density. To overcome these issues, this study first derives analytical expressions for per-unit-length inductance and thrust force. Based on these, key electromagnetic parameters and structural parameters of the motor are designed. A segmented design scheme is also proposed. A finite element model of a bilateral long-stator PMSLM is then established using Ansys Maxwell. Simulations are performed to analyze the motor's back electromotive force (EMF), electromagnetic thrust force, inductance distribution, and induced voltage. The results show a good agreement between the simulation and theory. The error in inductance calculations ranges from −5.5% to +6.65%. The absolute error between the calculated and simulated thrust force values is below 0.8 kN. Furthermore, the non-uniformity in inductance distribution and the causes of thrust force fluctuation are investigated. Odd-order harmonics, such as the third and fifth, are identified in the induced voltage. This research offers a design methodology and simulation verification for ultra-high-speed PMSLMs. It lays a foundation for the future development of end-effect compensation and harmonic suppression strategies.

Keywords: ultra-high speed; permanent magnet; synchronous linear motor; inductance distribution; thrust force density; maglev

Check for updates

Academic Editor: Shuxiang Dong

Received: 5 June 2026
Revised: 27 June 2026
Accepted: 6 July 2026
Published: 16 July 2026

1. Introduction

With the development of the ultra-high-speed maglev transportation [1,2] and the ground high-speed testing for aircraft [3], the study of high thrust force density linear motors has gained increasing attention in recent years. Mainstream high-thrust force linear motors can be categorized into induction linear motors [4,5] and synchronous linear motors [6]. The use of an iron core can significantly increase air gap magnetic density due to its high permeability, thereby improving thrust force density and providing mechanical support. For this reason, in ultra-high-speed tests with tracks extending over kilometers, long-stator segmented structures are often employed [7]. Induction linear motors have a relatively simple structure and a lightweight mover. However, they suffer from low power factor, low efficiency, and limited thrust force density. In contrast, synchronous linear motors offer higher power density, better power factor, and improved efficiency. Synchronous linear motors offer superior control precision, making them well-suited for ultra-high-speed traction. High-speed maglev trains use a single-sided stator configuration, where the traction and levitation systems are coupled [8]. This integrated structure demands a highly sophisticated control system, posing challenges in ultra-high-speed scenarios. A bilateral stator configuration can more effectively utilize the magnetic field of the permanent magnets to enhance thrust force density. Japan's superconducting electrodynamic suspension system employs superconductors [9], which entail relatively high costs. In comparison, using multi-pole permanent magnets as the mover offers a simpler structure and lower cost. Based on these considerations, this paper focuses on the preliminary design of the ultra-high-speed bilateral permanent magnet synchronous linear motor.

Accurate modeling of electromagnetic fields is essential for the preliminary design of ultra-high-speed PMSLMs, primarily relying on analytical and numerical methods. Reference [10] developed a mathematical model based on stator current orientation in the synchronous reference frame, incorporating core saturation to derive magnetic field distributions and thrust force formulas. Reference [11] established a two-dimensional finite element model, calculating flux density using Ampère's law and determining thrust and normal forces via the Maxwell stress method. Reference [12] employed an equivalent magnetization model with Fourier series expansion to compute air gap flux density and the Lorentz force law, and validated results using finite element analysis. Reference [13] used the Biot–Savart law and Poisson's equation to model the magnetic field of a Halbach array and verified end effects via finite element analysis (FEA); In addition, the thrust force, normal force, back EMF, and thrust force ripple are also analyzed using the Maxwell stress tensor and dynamic circuit theory. Reference [14] introduced a double Fourier series method to analytically solve the three-dimensional magnetic field, validated it with FEA, and also derived thrust and normal force expressions using the virtual work principle. Reference [15] combined dynamic circuit theory and virtual displacement methods to build a three-dimensional analytical model based on the Biot–Savart law, calculating electromagnetic forces via the Maxwell stress tensor and Lorentz force integration. Current research also focuses on thrust force ripple analysis and suppression. Reference [16] proposed an efficient pseudo-3D analytical model for double-sided (bilateral) linear induction motors, accounting for longitudinal, transverse, and exit-end effects. Reference [17] studied the electromagnetic performance of linear motors for ultra-high-speed maglev under square-wave voltage supply and proposed optimization strategies. Reference [18] achieved high thrust force and low ripple using fractional-slot windings and innovative permanent magnet arrangements. Reference [19] introduced an interleaved laminated coil structure that reduced force ripple to 2.3% under the PWM supply. Control strategies [20,21] and advanced algorithms [22] also remain effective for thrust force fluctuation suppression. Although progress has been made in electromagnetic modeling and thrust force analysis, existing models are often not suitable for rapid estimation of fields and forces in the segment design of long-stator linear synchronous motors. By neglecting secondary factors such as winding cross-section shape and tooth-slot dimensions, the modeling process can be simplified, thereby easing the motor design procedure.

Based on the above, this study concentrates on the bilateral permanent magnet synchronous linear motor. We develop both inductance and electromagnetic force models

https://doi.org/10.3390/act15070400

and propose a simplified preliminary design flow. First, by neglecting end effects, cogging effects, and detailed winding geometry, we establish analytical formulas for per-unit-length inductance and thrust force under multi-motor parallel operation. Second, we analyze the influence of key structural parameters—air gap length and pole pitch—on inductance, thrust force, and their interrelationship. Finally, a finite element model is built to compare theoretical and simulated inductance values and to validate the accuracy of the thrust force formula.

The main contribution of this work is that the proposed magnetic field model accommodates any number of parallel motor units, broadening its applicability. The derived per-unit-length expressions for inductance and thrust force are concise, making them more suitable for rapid preliminary designs compared to numerical simulations or complex analytical solutions.

2. Modeling of the Ultra-High-Speed PMSLM

Considering the high thrust force requirements of ultra-high-speed PMSLMs, this paper discusses the structure of a bilateral long-stator permanent magnet synchronous linear motor, as shown in Figure 1. The tooth slots and winding regions are defined as current layers to reduce the number of solution regions and simplify the physical model. The following assumptions are adopted under the low-frequency (quasi-static) approximation:

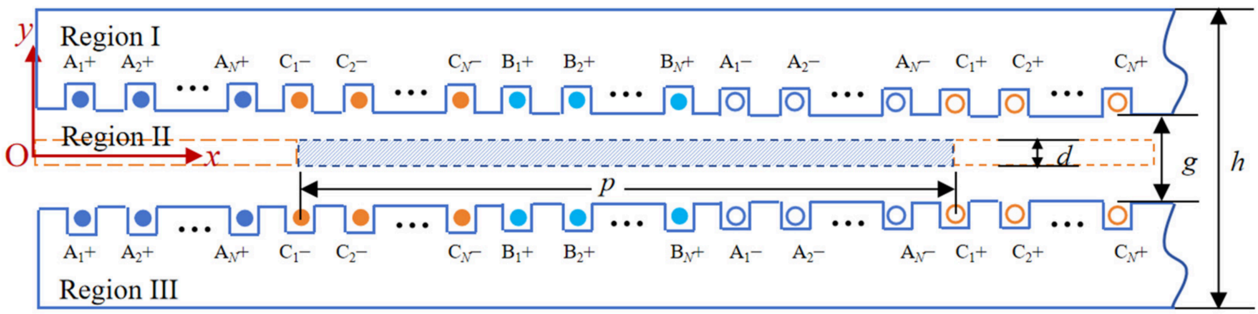

Figure 1. A schematic diagram of the long-stator linear motor structure.

(1) The iron core is infinitely thick;
(2) The magnetic field does not change along the z-axis;
(3) The movers' material is NdFeB;
(4) Ignoring end effects and skin effect;
(5) Teeth and slot effects are ignored.

As shown in Figure 1, the long-stator linear motor adopts a bilateral symmetric structure, and the position of the mover is shown by the dashed line. The winding ports are arranged in the order A_1+, A_2+, ..., A_N+, C_1-, C_2-, ..., C_N-, B_1+, B_2+, ..., B_N+. A positive sign indicates the current flows out of the paper, while a negative sign indicates the current flows into the paper. To reduce harmonics, the phase difference between two adjacent ports is $\pi/(3N)$. A_k+, C_k-, B_k+ ($k = 1, 2, \ldots N$) adopt the same power supply configuration as a three-phase motor. The stator core employs a laminated structure, with eddy current effects neglected and maintained in a non-saturated state. A Cartesian coordinate system (Oxy) is established with the x-axis aligned horizontally and the y-axis vertically. After removing the mover, the computational domain is divided into three regions: regions I and III represent ferromagnetic areas exhibiting a symmetrical electromagnetic field distribution along the x-axis, while the remaining region constitutes the air region II.

https://doi.org/10.3390/act15070400

2.1. Governing Equations

For the ferromagnetic region I, assume the current expressions for ports A_k+, B_k+, and C_k+ (k = 1, 2, . . ., N) are as follows:

$$\begin{cases} i_{A_k} = I_0 \sin\left(\omega t + \frac{\pi(k-1)}{3N}\right) \\ i_{B_k} = I_0 \sin\left(\omega t + \frac{\pi(2N+k-1)}{3N}\right) \\ i_{C_k} = I_0 \sin\left(\omega t + \frac{\pi(4N+k-1)}{3N}\right) \end{cases}, \tag{1}$$

where I_0 denotes the amplitude and ω the angular frequency of the current. At this time, the traveling wave magnetic field generated by the winding current moves toward the negative x-axis. Then, the spatial distribution of the current at the boundary between region I and region III is

$$I(x,t) = \sum_{k=-\infty}^{+\infty} I_0 \sin\left(\frac{\pi}{p}x + \omega t\right)\delta\left(x - \frac{(k-1)p}{3N}\right), k \in \mathbb{N}, \tag{2}$$

where $\delta(\cdot)$ represents the spatial impulse function and satisfies

$$\lim_{\varepsilon \to 0} \int_{\frac{(k-1)p}{3N}-\varepsilon}^{\frac{(k-1)p}{3N}+\varepsilon} \delta\left(x - \frac{(k-1)p}{3N}\right)dx = 1, k \in \mathbb{N}, \tag{3}$$

Taking t = 0, the current distribution exhibits odd symmetry with respect to the origin. According to the Fourier series, Equation (2) can be expanded as follows:

$$I(x,0) = \sum_{n=1}^{\infty} a_n \sin\frac{n\pi x}{p}, \tag{4}$$

where n takes an integer value indicating the order; the coefficient for each order a_n is expressed as

$$a_n = \frac{1}{p}\int_0^{2p} \sum_{k=0}^{3N} I_0 \sin\left(\frac{\pi}{p}x\right)\delta\left(x - \frac{(k-1)p}{3N}\right) \sin\frac{n\pi}{p}x dx, \tag{5}$$

It was calculated that $a_1 = 3NI_0/p$, and the coefficients of the other orders are zero. Then the distribution of current at the boundary between region I and region II is

$$I(x,0) = 3N \sin\frac{\pi x}{p} = \mathrm{Im}\left\{3\frac{NI_0}{p}e^{\mathrm{j}\frac{\pi}{p}x}\right\} \tag{6}$$

where j is the imaginary unit and $k = \pi/p$. For the vector magnetic potential of both region I and region III in the two-dimensional model, only the z-axis component exists; no free current exists in air region II, so a scalar magnetic potential can be used for electromagnetic field description. The electromagnetic field governing equations of region I and region II are, respectively,

$$\left(\frac{\partial^2}{\partial x^2} + \frac{\partial^2}{\partial y^2}\right)A_z^{\mathrm{I}}(x,y,t) = 0 \tag{7}$$

$$\left(\frac{\partial^2}{\partial x^2} + \frac{\partial^2}{\partial y^2}\right)\varphi^{\mathrm{II}}(x,y,t) = 0 \tag{8}$$

where $A_z^{\mathrm{I}}(x,y,t)$ and $\varphi^{\mathrm{II}}(x,y,t)$ can be expressed in the form of $\mathrm{e}^{\mathrm{j}(kx+\omega t)}$, respectively representing the vector magnetic potential of region I and the scalar magnetic potential of region II. The vector magnetic potential of region III is similar to the description of region I.

2.2. Boundary Conditions

For simplicity, it is assumed that the magnetic field strength on the surface of the iron core is zero. That is

$$A_z^{\mathrm{I}}(x,h/2,t)=0 \tag{9}$$

At the boundary between region I and region II, the following conditions apply:

$$-\frac{\partial A_z^{\mathrm{I}}(x,g/2,t)}{\partial x}=-\mu_0\frac{\partial\varphi^{\mathrm{II}}(x,g/2,t)}{\partial y} \tag{10}$$

$$-\frac{1}{\mu}\frac{\partial A_z^{\mathrm{I}}(x,g/2,t)}{\partial y}-\mu_0\frac{\partial\varphi^{\mathrm{II}}(x,g/2,t)}{\partial x}=I(x,t) \tag{11}$$

where μ_0 is the permeability of air and μ is the core's permeability. Additionally, it is necessary to supplement the symmetry condition:

$$\frac{\partial\varphi^{\mathrm{II}}(x,0,t)}{\partial x}=0 \tag{12}$$

2.3. Inductance Coefficient and Thrust Force Density

According to Equations (1)–(12), the per-unit-length inductance can be evaluated as

$$L=-\frac{1}{2p}\frac{1}{I(x,0)}\int_0^p\mu_0\frac{\partial\varphi^{\mathrm{II}}(x,g/2,0)}{\partial y}wdx=4.8N\frac{w}{p}\frac{\mathrm{e}^{kg/2}}{\left(e^{kg/2}-\mu_{\mathrm{r}}e^{2kd-kg/2}\right)} \tag{13}$$

For PMSLMs, a larger horizontal magnetic field component on the mover's surfaces results in a greater thrust force. Using the magnetic charge method, the surface magnetic charge density of the mover is $\sigma_{\mathrm{m}} = B_{\mathrm{r}}/\mu_0$, where B_{r} is the remanent flux density. Ignoring the effect of the mover on the horizontal magnetic field component on its surface, the x-directed magnetic field component at $y = d/2$ is

$$H_{\mathrm{x}}^{\mathrm{II}}(x,y,t)=-\frac{\partial\varphi^{\mathrm{II}}(x,y,t)}{\partial x}\approx\mathrm{Re}\left\{-\frac{I_0(\mathrm{e}^{kd/2}-\mathrm{e}^{-kd/2})}{(\mathrm{e}^{kg/2}-\mathrm{e}^{-kg/2})}\mathrm{e}^{\mathrm{j}(kx+\omega t)}\right\} \tag{14}$$

Then the approximate expression for the maximum per-unit-length thrust force is

$$f_{\mathrm{x}}=\frac{-2w\sigma_{\mathrm{m}}}{p}\int_0^p\frac{\partial\varphi^{\mathrm{II}}(x,d/2,0)}{\partial x}dx\approx\frac{12wB_{\mathrm{r}}NI_0}{\pi p}\frac{(\mathrm{e}^{kd/2}-\mathrm{e}^{-kd/2})}{(\mathrm{e}^{kg/2}-\mathrm{e}^{-kg/2})} \tag{15}$$

3. Influence of Structural Parameters on Electromagnetic Parameters

In the mainstream design of ultra-high-speed traction systems, the number of parallel motors is four. The inductance density for per-unit thickness core is defined as the inductance coefficient, and the thrust force density for per-unit residual magnetism, per-unit current, and per-unit core thickness is defined as the thrust force coefficient.

3.1. Inductance Coefficient

Equation (13) indicates that the inductance coefficient is proportional to the number of parallel motors and is influenced by the pole pitch (p) and air gap (g). To investigate the coupling effect of pole pitch and air gap, the air gap is varied from 20 mm to 100 mm. The inductance coefficients under different pole pitches (100 mm, 200 mm, 300 mm, 400 mm, 500 mm) are shown in Figure 2.

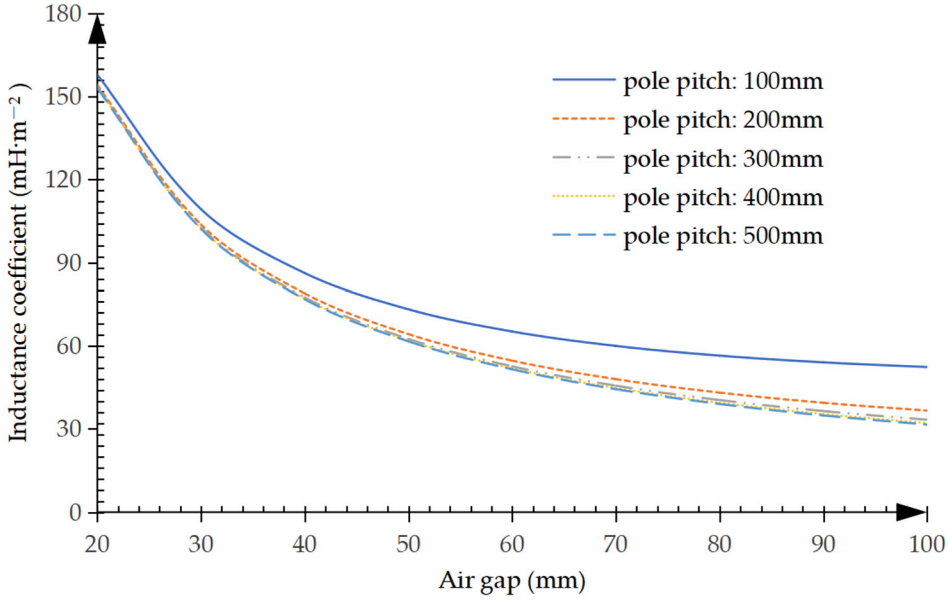

Figure 2. Variation in the inductance coefficient with the air gap under different pole pitches.

3.2. Thrust Force Coefficient

Equation (15) shows that the thrust density is proportional to the PM remanence (B_r), the number of parallel motors (N), and the current amplitude (I_0). It varies approximately exponentially with PM thickness. With the PM thickness fixed at 30 mm and the air gap varying from 50 mm to 100 mm, the thrust coefficient under different pole pitches is shown in Figure 3.

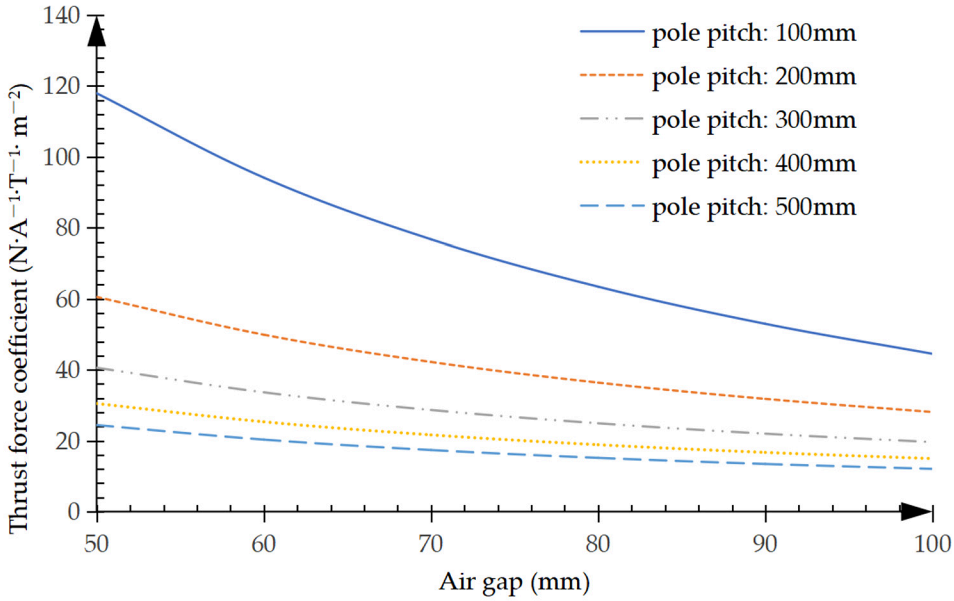

Figure 3. Variation in the thrust force coefficient with the air gap under different pole pitches.

It reveals that the thrust coefficient decays with the increasing air gap. For any pole pitch, the thrust force coefficient exhibits near-exponential decay as the air gap increases. The decay rate slows with larger pole pitches. This is due to the increased magnetic reluctance reducing the main flux. The pole pitch regulates the sensitivity of the thrust force coefficient. Larger pole pitches result in flatter decay curves, indicating reduced sensitivity to air gap variations. This suggests large-pole-pitch designs offer stable outputs and better robustness against air gap fluctuations. The thrust force coefficient is inversely proportional to pole pitch. At g = 50 mm, thrust force coefficients are 117.9 N/m^2, 60.6 N/m^2, 40.6 N/m^2, 30.5 N/m^2, and 24.4 N/m^2 for pole pitches of 100 mm, 200 mm, 300 mm, 400 mm, and 500 mm respectively. A fivefold increase in pole pitch reduces thrust force coefficients to about one-fifth. This is primarily because larger pole pitches disperse the main flux, reducing the air gap flux density and thus reducing the electromagnetic thrust force.

In summary, designing a PMSLM with low inductance and high thrust force requires balancing the pole pitch and air gap.

4. Performance Calculation of Ultra-High-Speed PMSLMs

The amplitude of the per-unit-length back electromotive force for a single-phase winding is

$$e_{\mathrm{v}} = -\frac{\mu_0 w v}{p} \cdot \frac{\partial \varphi^{\mathrm{II}}(x, g/2, t)}{\partial y} \tag{16}$$

The amplitude of the induced voltage per unit length is

$$e_{\mathrm{i}} = 2\pi f L I_0 \tag{17}$$

Assuming that the cross-sectional area of each winding is S, the amplitude of the resistance voltage drop per unit length is

$$e_{\mathrm{r}} = \frac{3N\rho w I_0}{pS} \tag{18}$$

Neglecting feeder cable effects, suppose that bilateral stator windings are connected in series and supplied by two inverters in series. Given the mover length l_{v} and stator segment length l_{i}, the inverter output voltage for a single side is

$$U_{\mathrm{s}} = \sqrt{(E_{\mathrm{v}} + E_{\mathrm{r}})^2 + E_{\mathrm{i}}^2} = \sqrt{(l_{\mathrm{v}} e_{\mathrm{v}} + l_{\mathrm{i}} e_{\mathrm{r}})^2 + (l_{\mathrm{i}} e_{\mathrm{i}})^2} \tag{19}$$

The motor’s power factor is

$$\cos\varphi = \frac{E_{\mathrm{r}} + E_{\mathrm{v}}}{U_{\mathrm{s}}} \tag{20}$$

The motor’s efficiency is

$$\eta = \frac{E_v}{E_r + E_v} \tag{21}$$

5. Preliminary Design of Ultra-High-Speed PMSLM

The ultra-high-speed maglev test requires accelerating a load to an ultra-high speed within a short distance. The design target is to accelerate a 650 kg load to 1500 km/h within 500 m. The preliminary design will refer to China’s 600 km/h high-speed maglev PMSLM design standards:

(1) Single-phase winding insulation strength: 6 kV;
(2) Operating current (RMS at high frequency): 1.2 kA;
(3) Inverter output frequency ranges: 0~356 Hz.

5.1. Preliminary Design of Key Parameters

The pole pitch of the linear motor of the high-speed maglev is 0.258 m. Without altering the output frequency of the converter and the insulation strength of the cable, the selected pole pitch is

$$p = \frac{1500\ \mathrm{km/h}}{600\ \mathrm{km/h}} \times 0.258\ \mathrm{m} = 0.645\ \mathrm{m} \tag{22}$$

Referring to the rated air gap of the high-speed maglev, the air gap between the mover and stator is designed to be 10 mm. The stator stack thickness is 450 mm, and the height is 90 mm. Stator slots and teeth are of equal width.

Assuming a constant acceleration of the mover, the required thrust force is

$$F_0 = m\frac{v_{\max}^2}{2s} = 1.129 \times 10^5 \mathrm{N} \tag{23}$$

where $v_{\max}$ denotes the maximum speed of 416.7 m/s and s is the total length of the track of 500 m.

As shown in Equation (15), the thrust force density exhibits a positive correlation with the thickness of the permanent magnet (mover). The height of the permanent magnet must first satisfy the thrust force density requirement. Meanwhile, its thickness should match that of the stator stack. In this design, a permanent magnet with a thickness of 50 mm and a grade of N52 is selected. The length of each individual permanent magnet pole corresponds to the pole pitch. The number of poles must be determined to meet the total thrust force requirement. When the RMS value of the phase winding current is set to 1200 A, the thrust force provided by a single permanent magnet pole can be calculated as follows:

$$F_{\mathrm{p}} = p \cdot f_{\mathrm{x}} = 1.181 \times 10^4 \mathrm{N} \tag{24}$$

Obviously, 10 poles of the mover are required to meet the thrust force requirements. In this case, the length of the mover is calculated by l_{v} = 10 × 0.645 m = 6.45 m. When the number of parallel motors is four, the design parameters of the PMSLM are shown in Table 1.

Table 1. The main parameters of the PMSLM.

Parameters	Values	Units
Air gap	10	mm
Pole pitch	645	mm
Groove width	26.875	mm
Stator stack's cross-section	450 × 90	mm^2
Winding's cross-section	285	mm^2
Operating current (RMS)	1200	A
Permanent magnet grade	N52	-
Mover height	50	mm
Number of mover poles	10	-

5.2. Preliminary Design of Motor Sections

For linear motors, a reduced number of segments leads to fewer switching devices. This reduction is beneficial for lowering overall system costs. Therefore, it is critical to maximize the terminal voltage and improve the power factor as much as possible. Two methods are commonly used for segmenting the linear motor.

(a) The first method begins from the initial stator segment. The length of the first segment and its terminal velocity are determined based on the voltage limitations and current magnitudes of each phase. Subsequent stator segments are then designed sequentially in a downstream direction.

(b) The second method starts from the final stator segment. The length and the entry velocity of the last segment are defined according to the voltage constraint, current amplitude, and maximum operational speed of each phase. Preceding segments are then designed sequentially in an upstream direction.

In both methods, the phase voltage must adhere to insulation requirements. Its amplitude should remain below 6 kV. When neglecting the impact of feeder cables and switching delays, the length of each stator segment must satisfy the condition specified in Equation (25).

$$U_\mathrm{s} \leq 6000\mathrm{V} \tag{25}$$

When the first method is adopted, the length of the initial stator segment is first determined using Equation (25). Subsequently, the terminal speed of this segment is calculated based on Equation (26).

$$v_n = \sqrt{v_{n-1}^2 + 2al_n} \tag{26}$$

When the second method is adopted, the terminal speed of the final motor segment is known. Based on this, the length of the end stator segment can be determined using Equation (25). Subsequently, the speed of the mover passing each terminal end of the stator can be derived from Equation (27). By iteratively applying Equations (25) and (27), the lengths of all preceding stator segments can be sequentially computed.

$$v_{n-1} = \sqrt{v_n^2 - 2al_n} \tag{27}$$

Based on the above analysis, the stator length, voltage drop, power factor, and efficiency for each segment can be determined. The segmentation results according to the two methods are detailed in Tables 2 and 3, respectively. A comparative analysis reveals distinct characteristics: (1) The first method exhibits a "long-front, short-rear" configuration. The initial segment measures 156.090 m in length, while the final segment is significantly shorter at 36.120 m. (2) The second scheme demonstrates a more balanced length distribution. Segment lengths range between 73.530 m and 135.450 m. The terminal segment is 86.430 m. Regarding electrical performance: (1) In the first scheme, the stator voltage remains slightly below 6 kV for the first four segments. The fifth segment experiences a notable drop to 2.469 kV. (2) In the second scheme, the voltage is 1.835 kV in the first segment but remains consistently around 6 kV for the subsequent segments. Both methods exhibit relatively low power factors. The first method yields a marginally lower power factor only in the initial segment compared to the second method. In segments 2 to 5, the first method demonstrates superior power factor performance. From a practical perspective, the balanced segment length distribution in the second scheme facilitates manufacturing and installation processes. The reasonable length of the final segment enables more precise control during high-speed operation.

Table 2. Segment design by Method 1.

Segment Number	1	2	3	4	5
Length (m)	10	156.090	117.390	101.620	90.300
Terminal velocity (m/s)	645	232.805	308.153	360.411	401.560
Back EMF (V)	26.875	246.180	325.857	381.117	424.630
Induction voltage (kV)	450 × 90	5.958	5.931	5.945	5.945

Table 2. *Cont.*

Segment Number	1	2	3	4	5
Terminal voltage (kV)	285	5.963	5.940	5.958	5.960
Power factor	1200	0.041	0.055	0.064	0.071
Length (m)	10	156.090	117.390	101.620	90.300

Table 3. Segment design by Method 2.

Segment Number	1	2	3	4	5
Length (m)	73.530	135.450	119.650	95.460	86.430
Terminal velocity (m/s)	159.219	269.039	332.348	378.947	416.667
Back EMF (V)	168.367	284.496	351.442	400.718	440.605
Induction voltage (kV)	1.919	5.974	5.975	5.931	5.904
Terminal voltage (kV)	0.087	0.048	0.059	0.067	0.074
Power factor	73.530	135.450	119.650	95.460	86.430
Length (m)	159.219	269.039	332.348	378.947	416.667

6. Finite Element Simulation and Analysis

A finite element model of a bilateral long-stator PMSLM was developed using Ansys Maxwell software. The mover comprises five magnetic poles. The overall span of the mover is 3.225 m. Both stator and rotor dimensions strictly matched the predefined design parameters. The stator core material is DW310_35, with balloon boundary conditions applied. The winding ports were assigned a mesh length of 3 mm, while the stator core mesh length was set to 30 mm, with automatic meshing applied to other regions.

The total length of the stator in the mover-removed model, as shown in Figure 4, is 3.252 m, and the stator winding excitation adopts the current source form. The simulation results are shown in Table 4. Note that the winding is arranged in the order A_1+, A_2+, A_3+, A_4+, C_1-, C_2-, C_3-, C_4-, B_1+, B_2+, B_3+, B_4+. Table 4 presents the inductance values of the 12-phase winding. The results show the inductance values initially increase and then decrease along the winding array. Spatially symmetric positions exhibit closely matched inductance values. For example, winding pairs A_1/B_4 and A_2/B_3 demonstrate nearly identical inductance values. The comparison between simulated and theoretical inductance values reveals a high agreement. The relative errors range from -5.501% to +6.650%, indicating high accuracy in the theoretical calculations, validating the reliability of the analytical model. End windings (A_1, B_4) show substantially lower inductance values compared to central windings (C_2, C_3). This phenomenon primarily results from the longitudinal end effect inherent in linear motor designs.

The total length of the stator in the mover-exist model is 13.572 m, and the electromagnetic field distribution and thrust force results are shown in Figures 5 and 6 respectively. Observations indicate significant magnetic leakage at the ends of the stator. This leakage causes field attenuation, reducing the air gap flux density when the mover passes the stator terminals. Consequently, the electromagnetic force decreases, with a minimum thrust force value of 26.875 kN. As the mover enters the central region of the stator, the magnetic field becomes uniform. This results in increased thrust force, reaching a peak value of 38.807 kN. Thrust force exhibits considerable fluctuation during operation. The fluctuation amplitude peaks at 23.123% of the average thrust force value. The primary fluctuation frequency occurs at 24 times the supply frequency. This phenomenon is caused by periodic alignment and misalignment between the stator's teeth and the mover during operation. Fourier transform analysis was performed on the thrust force data, and the resulting spectrum is shown in Figure 7. The component 31.519 kN at zero frequency, representing the average thrust force. A 24th-order harmonic component with an amplitude of 3.537 kN, accounting for 11.221% of the average thrust force. Calculated theoretical thrust force (70 mm tooth spacing) yields 27.392 kN, showing an absolute error below 0.8 kN compared to the peak. When considering the distance between the winding geometric center and tooth surface, the theoretical thrust force (96.875 mm tooth spacing) yields 27.392 kN, with an absolute error under 0.6 kN. Both calculation methods demonstrate minimal discrepancies with simulation results.

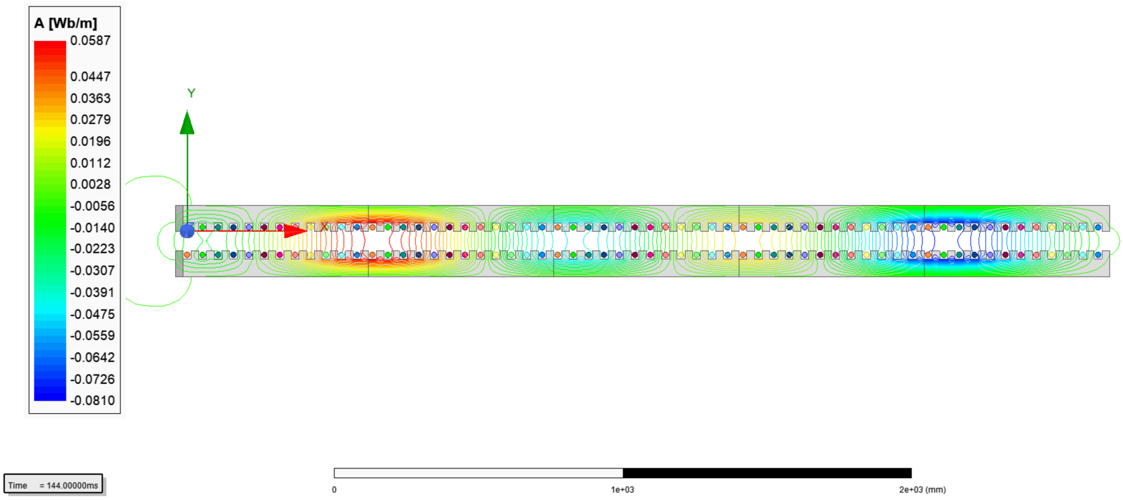

Figure 4. PMSLM model with the mover moved.

Table 4. Inductance values of each winding (theoretical inductance value: 19.834 μH$\cdot$m^{-1}).

Winding Name	A_1	A_2	A_3	A_4	C_1	C_2
Inductance (μH$\cdot$m^{-1})	18.745	19.448	20.082	20.600	20.965	21.153
Winding Name	C_3	C_4	B_1	B_2	B_3	B_4
Inductance (μH$\cdot$m^{-1})	21.153	20.964	20.599	20.082	19.447	18.743

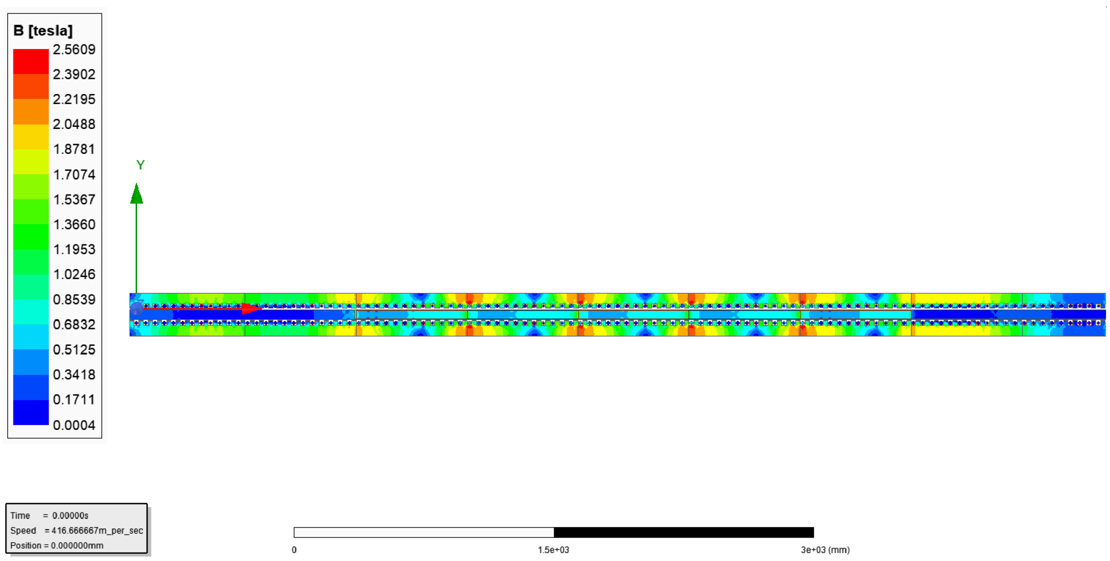

Figure 5. Mover-exist PMSLM model.

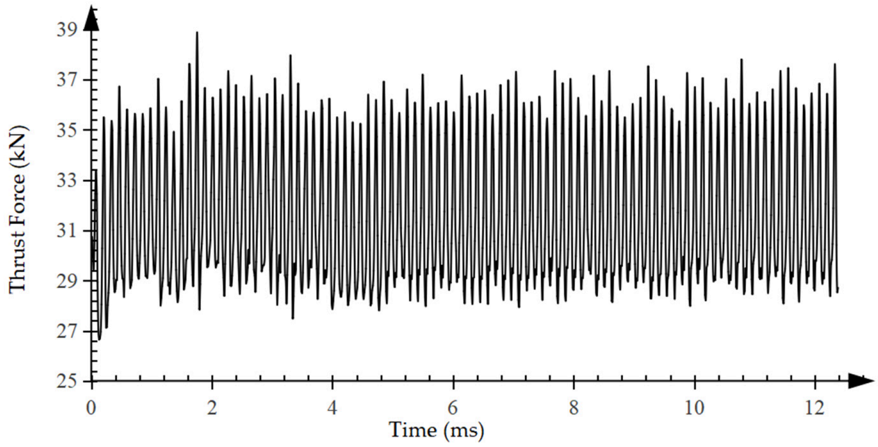

Figure 6. Time variation in thrust force during synchronous operation.

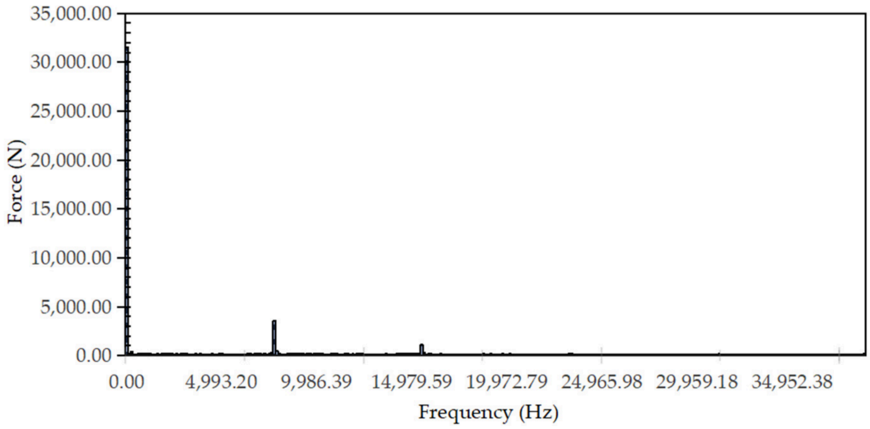

Figure 7. Frequency spectrum characteristics of the thrust force.

Figure 8 illustrates the voltage waveform of the phase windings. The waveform exhibits periodic fluctuations between +3 kV and −3 kV. Its cycle duration matches the power supply frequency. A consistent phase angle difference of $\pi/12$ is maintained between adjacent phases. Waveform distortion primarily originates from core saturation effects. This saturation introduces nonlinearity into the magnetization curve, deviating from ideal sinusoidal behavior. Consequently, harmonic components are generated.

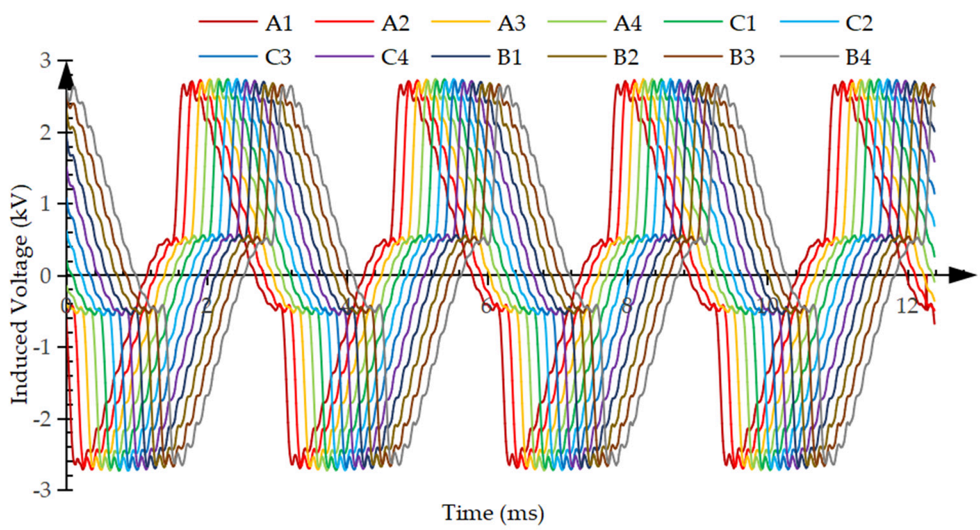

Figure 8. Variation in the induced voltage over time.

Figure 9 displays the harmonic spectrum analysis. Dominant spectral components are observed at 323.102 Hz (fundamental frequency) with amplitude 2.105 kV, 969.305 Hz (3rd harmonic) with amplitude 0.463 kV, and 1615.509 Hz (5th harmonic) with amplitude 0.270 kV. Higher-frequency components show progressively diminishing amplitudes. Although these high-frequency harmonics have relatively low amplitudes, they contribute to increased iron and copper losses. Therefore, minimizing current harmonic components is essential for optimizing linear motor performance.

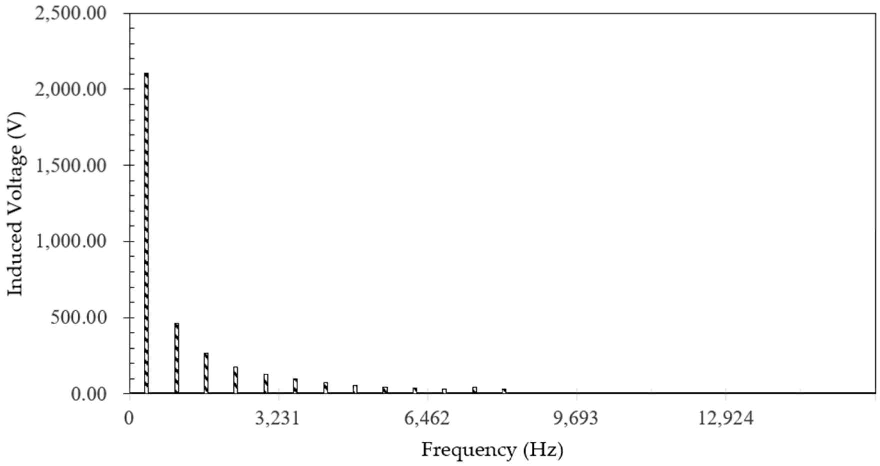

Figure 9. Frequency spectrum characteristics of induced voltage.

7. Conclusions

This research addresses the core requirements of high thrust force density and low inductance in PMSLMs for ultra-high-speed traction. A systematic investigation was conducted, spanning electromagnetic theoretical modeling, parameter design, and finite element validation. The main conclusions are as follows.

(a) An analytical model neglecting end effects was established. Formulas for the inductance coefficient and thrust force coefficient were derived. Finite element simulations confirmed small errors between theoretical and simulated values for winding inductance and electromagnetic force. This validates the model's accuracy and reliability, providing a theoretical tool for rapid preliminary design and optimization of ultra-high-speed linear motors.

(b) This study reveals the coupling effects of pole pitch and air gap on electromagnetic parameters. For large air gaps, increasing the pole pitch effectively reduces the inductance. Larger pole-pitch designs enhance thrust force robustness against air gap fluctuations.

(c) Two segmentation strategies were compared: the "long front, short rear" delivering superior overall power factor; the "balanced-length" configuration simplifies manufacturing, installation, and ultra-high-speed control.

(d) Longitudinal end effects cause a non-uniform spatial distribution of winding inductance. Cogging effects induce significant thrust force fluctuations. Induced voltage waveforms contain prominent 3rd and 5th harmonics, increasing core losses.

This study establishes a complete PMSLM design methodology, integrating theoretical calculation, parameter analysis, and simulation verification. The proposed motor scheme achieves ultra-high-speed acceleration of loads over short distances, offering significant engineering value for advancing maglev traction systems.

Author Contributions: Writing—original draft, Y.H., D.G. and T.W.; formal analysis, K.H.; supervision, Y.Z., J.X. and G.L. All authors have read and agreed to the published version of the manuscript.

Funding: This research was funded by the Key Projects of National Natural Science Foundation of China, grant numbers 52432012, 52232013, and 52332011; the Research Project of the China Academy of Railway Science, grant number KYL202411-0134; the Sichuan Provincial Natural Science Foundation Project, grant number 24NSFSC7137; and the Open Foundation of the State Key Laboratory of High-speed Maglev Transportation Technology, grant number SKLM-SFCF-2023-010.

Data Availability Statement: Data are contained within the article.

Conflicts of Interest: The authors declare no conflicts of interest.

Abbreviations

The following abbreviations are used in this manuscript:

PMSLM	Permanent magnet synchronous linear motor
EMF	Electromotive force
FEA	Finite element analysis
RMS	Root mean square

References

1. Wang, Z.; Long, Z.; Li, X. Levitation control of permanent magnet electromagnetic hybrid suspension maglev train. *Proc. Inst. Mech. Eng. Part I J. Syst. Control Eng.* **2018**, *232*, 315–323. [CrossRef]
2. Liang, S.; Zhai, M.; Long, Z. Parameter Impact Analysis and Vibration Control for High Speed Maglev Train-Track Coupling System with Experimental Verification. *IEEE Trans. Veh. Technol.* **2025**, *74*, 10282–10296. [CrossRef]
3. Hu, Y.; Chen, B.; Lin, G.; Wang, Z. Three-Dimensional Modelling and Validation for the Ultra-High-Speed EDS Rocket Sled with PM Halbach Array. *Actuators* **2025**, *14*, 225. [CrossRef]
4. Zhang, L.; Xie, X.; Wu, D.; Wang, Z.; Wang, J.; Jing, J.; Deng, H.; Li, J.; Huang, J.; Huang, J. Cascade Nonlinear Observer-Based Speed-Sensorless Adaptive Twisting Sliding Mode Control of Linear Induction Motor. *Actuators* **2025**, *14*, 318. [CrossRef]
5. Hu, H.; Yu, S.; Ren, L.; Zhai, M.; Chen, Y. Improved Interconnected MRAS Parameter Identification for Speed Sensorless Control of Linear Induction Motor. *Actuators* **2025**, *14*, 2.
6. Zhao, Y.; Ren, Z.; Lin, G.; Ren, S.; Wang, H.; Zhang, Z.; Ren, L. Enhanced Decoupling Control for High-Speed Maglev Linear Synchronous Motor Using Complex Vector with Compensation Factors. *J. Electr. Eng. Technol.* **2026**, *21*, 769–783.
7. Wang, Y.; Shi, L.; Xu, F. A Fast Subblock Switch Strategy for Segmented Long Primary Linear Machines Based on an Asymmetric Parallel Topology. *IEEE Trans. Ind. Electron.* **2025**, *72*, 2380–2391. [CrossRef]
8. Dai, C.; Luo, G.; Long, Z. Research on Decoupling Problem of Suspension Gap and Location of Relative Position Sensor in High Speed Maglev Train. *IEEE Access* **2019**, *7*, 29836–29844. [CrossRef]
9. Huang, H.; Cheng, Y.; Li, H.; Li, H.; Deng, Z.; Zheng, J.; Lin, G. Experimental Platform Design and Transient Guidance Force Analysis for Cross-Connected Null-Flux Coil Type Electrodynamic Suspension System. *IEEE Trans. Energy Convers.* **2026**, *41*, 1209–1221. [CrossRef]
10. Zhong, Z.; Shao, Z.; Yang, M.; Wang, X.; Xiao, Q.; Wang, Y. Quasi-Synchronous Operation Principle of a Variable Air-Gap Doubly Fed Linear Motor for High-Speed Maglev Application. *IEEE Trans. Transp. Electrif.* **2023**, *9*, 2929–2940. [CrossRef]
11. Ozturk, U.K.; Abdioglu, M.; Ozkat, E.C.; Mollahasanoglu, H. Extended 2-D Magnetic Field Modeling of Linear Motor to Investigate the Magnetic Force Parameters of High-Speed Superconducting Maglev. *IEEE Trans. Appl. Supercond.* **2023**, *33*, 3600508. [CrossRef]
12. Zhang, Z.; Luo, M.; Duan, J.; Kou, B. Design and Analysis of a Novel Frequency Modulation Secondary for High-Speed Permanent Magnet Linear Synchronous Motor. *IEEE/ASME Trans. Mechatron.* **2022**, *27*, 790–799. [CrossRef]
13. Liao, Z.; Yue, J.; Lin, G. Application Research of HTS Linear Motor Based on Halbach Array in High Speed Maglev System. *IEEE Trans. Appl. Supercond.* **2021**, *31*, 3600707. [CrossRef]
14. Lv, G.; Zhang, Z.; Liu, Y.; Zhou, T. Characteristics Analysis of Linear Synchronous Motor Integrated with Propulsion, Levitation, and Guidance in High-Speed Maglev System. *IEEE Trans. Transp. Electrif.* **2021**, *7*, 3185–3193. [CrossRef]
15. Zhao, Z.; Xu, S.; Liu, K.; Yang, W.; Li, J.; Ma, G. 3-D Analytical Model of Racetrack HTS Coil Subject to Travelling Magnetic Fields. *J. Supercond. Nov. Magn.* **2021**, *34*, 75–84. [CrossRef]
16. Rametti, S.; Pierrejean, L.; Hodder, A.; Paolone, M. Pseudo-Three-Dimensional Analytical Model of Linear Induction Motors for High-Speed Applications. *IEEE Trans. Transp. Electrif.* **2024**, *10*, 9109–9120. [CrossRef]

17. Gao, H.; Shi, T.; Gao, X.; Lei, Y.; Yan, D.; Guo, L.; Yan, Y. Electromagnetic characteristic analysis and design of a linear motor used for ultra-high-speed EMS maglev train. *Sci. China Technol. Sci.* **2024**, *67*, 1957–1973. [CrossRef]
18. Wu, D.; Xu, J.; Lin, H. Research on High Thrust Force Characteristics with Proper Fractional-Slot Concentrated Winding for a Ultra-Low Speed Tubular PM Linear Machine. *IEEE Trans. Appl. Supercond.* **2024**, *34*, 5206206. [CrossRef]
19. Dong, F.; Hao, L.; Park, D.; Iwasa, Y.; Huang, Z. On the future sustainable ultra-high-speed maglev: An energy-economical superconducting linear thrusting system. *Energy Convers. Manag.* **2023**, *291*, 117247. [CrossRef]
20. Gao, Z.; Ge, Q.; Li, Y.; Zhao, L.; Zhang, B.; Wang, K. Hybrid Improved Carrier-Based PWM Strategy for Three-Level Neutral-Point-Clamped Inverter with Wide Frequency Range. *IEEE Trans. Power Electron.* **2021**, *36*, 8517–8538. [CrossRef]
21. Ma, Z.; Niu, H.; Zhang, X.; Wu, X.; Cai, X. Virtual Space Vector Overmodulation Strategy for NPC Three-Level Inverters with Common-Mode Voltage Suppression. *IEEE Trans. Power Electron.* **2024**, *39*, 6877–6888. [CrossRef]
22. Xu, Y.; Zhao, Z.; Luo, H.; Li, L. Data-driven control performance degradation recovery as an extension of loop transfer recovery. *Automatica* **2025**, *174*, 112110. [CrossRef]